Design and Scale-Up of Chemical Reactors for Nanoparticle Precipitation

Daniele L. Marchisio, Liliana Rivautella, and Antonello A. Barresi
Dipartimento di Scienza dei Materiali e Ingegneria Chimica—Politecnico di Torino, Torino, Italy

DOI 10.1002/aic.10786

In recent years there has been a growing interest in production on an industrial scale of particles with size in the sub-micron range (40-200 nm). This can be done by controlling particle formation in order to nucleate very small particles and by tailoring the particle surface in order to avoid particle aggregation and produce stable suspensions. In this work we focus on the role of turbulent mixing on particle formation in confined impinging jet reactors. In particular, we show how computational fluid dynamics and simple precipitation models could be used to derive scale-up criteria for the production of nanoparticles. © 2006 American Institute of Chemical Engineers *AIChE J,* 52: 1877–1887, 2006
Keywords: nanoparticles, CFD, modeling, precipitation, scale-up, confined impinging jet reactor, barium sulfate

Introduction

The main purpose of this work is to develop a methodology based on both experimental data and computational fluid dynamics (CFD) simulations for design, optimization, and scale-up of reactors suitable for producing solid particles with specific characteristics. In particular, we focus on the role of reactor size and fluid dynamics on particle size distribution (PSD), morphology, composition, and crystallinity.

Many applications of industrial interest exist, as diverse as production of nanoparticles of organic compounds and production of nano-structured ceramic materials. For example, the production of organic active nanoparticles with a polymeric coating for pharmaceutical applications is becoming increasingly important. These processes are based on the dissolution of an organic active and an amphiphilic diblock copolymer in an organic solvent that, after rapid mixing with a miscible anti-solvent, for example, water, precipitate.[1-3] The polymeric shell is added in order to avoid uncontrolled particle aggregation and further size-enlargement, or to increase the lifetime of particles into the bloodstream or to enhance drug retention.

Another important application is the production of metal oxides through standard precipitation or sol-gel processes.[4] In this case, the solid phase is produced by a chemical reaction and rapid mixing is crucial for controlling grain size and solid characteristics.[5]

Precipitation is the result of several mechanisms, namely, nucleation, molecular growth, and secondary processes, such as aggregation (or agglomeration) and breakage, and the driving force is super-saturation.[6] Nucleation is the formation of the solid phase and occurs when a critical number of molecules join together to form an embryo. Stable embryos form nuclei that grow into bigger particles through molecular growth. Nucleation and growth are competing phenomena since both consume solute molecules and, therefore, particle size is the result of this competition. Very small particles are produced by high nucleation rates whereas, on the contrary, big particles are produced by low nucleation rates.

Aggregation (or agglomeration) and breakage are defined as secondary processes since they are characterized by slower rates and, as a consequence, usually occur after particle formation; moreover, they do not consume solute molecules, leaving unchanged the total particle mass. Hereinafter with secondary processes we will refer only to particle aggregation since breakage is not significant in nanoparticle precipitation. Moreover, scale-up problems related to aggregation and breakage processes have already been investigated and results have been published elsewhere.[7]

Correspondence concerning this article should be addressed to D. Marchisio at daniele.marchisio@polito.it.

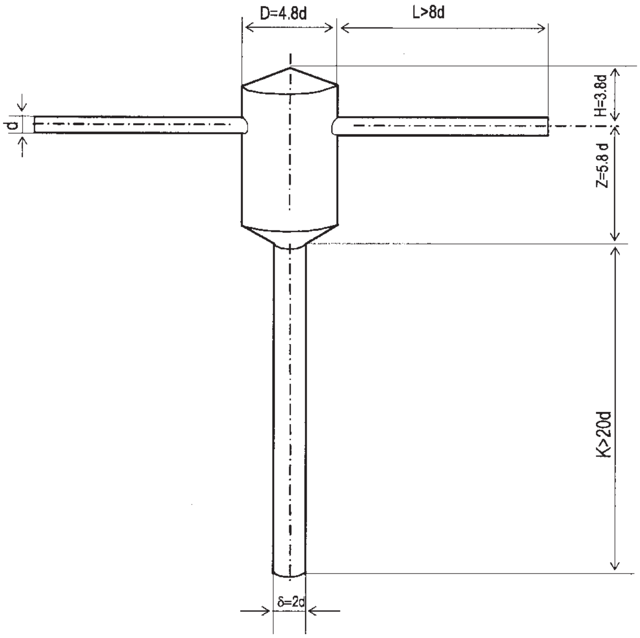

Figure 1. Reactor.

Aggregation also affects the PSD and, in fact, only if it is avoided can very small particles be produced.[8] Usually, nanoparticle aggregation is driven by Brownian motions; in fact, nanoparticles are less sensitive to turbulent fluctuations because of their very small size.[9] Moreover, particles interact through a combination of van der Waals attraction and electrostatic and steric repulsion forces[10]; and it is, therefore, clear that in order to prevent aggregation one must influence this balance. For example, using barium sulfate as a test material,[11-14] it was found that precipitation with a significant excess of one of the reactants (that is, barium ion) neutralizes aggregation, leading to stable suspensions.

Precipitation typically consists of (turbulent) mixing of two liquid streams and, therefore, mixing affects generation of super-saturation, influences its redistribution, and causes transport of previously formed particles in regions of high supersaturation. As already reported, small particles are produced by high nucleation rates, which can be obtained if high mixing rates are realized. Since precipitation processes are very fast, the effect of mixing is significant down to the micro-scale level and, therefore, nanoparticles can be produced in mixing devices characterized by extremely short contact and mixing time scales. Several reactors have been tested, such as T-tube or Y-tube,[8-11,15] reaching a characteristic mixing time of the order of milliseconds.

Another interesting alternative is the use of a confined impinging jets reactor (CIJR),[16,17] which consists of two high velocity linear jets of fluid that collide to rapidly reduce their scale of segregation within a small volume. Computational fluid dynamics (CFD) was used to quantify the mixing volume and plot the energy dissipation rate as a function of radial position in the impingement plane for free impinging jets.[18] An extensive comparison of the mixing performances of impinging jets versus those of a stirred tank reactor, a sliding surface mixing device, and a vortex reactor showed that the impinging jets mixer could be profitably used for precipitation since it ensures better process control, product reproducibility, and stability.[19] Also, the effect of the CIJR geometry on mixing and process performance by using a diazo-coupling competitive reaction scheme was studied and, assuming that the jets were free from the effects of chamber walls, it was possible to derive a correlation for the mixing time and a scaling model based on molecular diffusion and the Kolmogorov length-scale.[16] Mixing and reaction in a CIJR was also characterized, employing competitive reaction schemes; and testing different chamber geometries, jet diameters, fluid properties, and reaction rates, a correlation for the mixing time was proposed.[17]

The aim of this work is to investigate nanoparticle precipitation in CIJRs using barium sulfate as the test reaction. Two CIJRs are considered in this work with similar geometrical parameters but different sizes. Reactor performances are tested under different operating conditions (that is, jet velocities and reactant concentrations). Standard scale-up criteria based on the evaluation of the Damköhler number are used to interpret experimental data, and characteristic mixing and reaction times are evaluated by using CFD and a simplified precipitation model.

The article is organized as follows. First, the experimental set-up and the operating conditions are reported, and then the calculation of the time scale for mixing and precipitation is explained. Eventually, the relevant results are presented and discussed and some conclusions are drawn.

Experimental Setup and Operating Conditions

Precipitation experiments were carried out with barium sulfate at room temperature in two CIJRs. Aqueous solutions of barium chloride and sodium sulfate were fed to the reactor to form solid barium sulfate according to the following reaction:

$$\mathrm{BaCl_{2(aq)}} + \mathrm{Na_2SO_{4(aq)}} \rightarrow \mathrm{BaSO_{4(s)}} + \mathrm{2NaCl_{(aq)}}.$$

Aqueous solutions of barium chloride and sodium sulfate ($BaCl_2{\cdot}2H_2O$ and $Na_2SO_4{\cdot}10H_2O$ by Fluka-Cheminka) prepared with bi-distilled water (from reverse osmosis Millipore Milli-Q RG) were loaded into two syringes and fed into the reactor by using a high precision infusion pump (Kd Scientific).

The CIJR consists of two jets impinging and mixing in a small cylindrical chamber with conical head and outlet. Chamber diameter (D), chamber length ($H + Z$), outlet length (K), and diameter (δ) are multiples of the diameter jet (d), as indicated in Figure 1. As already reported in this work, two CIJRs with jet diameters equal to 1 and 2 mm were investigated. In Table 1 their characteristic dimensions are reported, and we will refer to them with the jet diameter.

Table 1. Characteristic Sizes of the Two Reactors Used in This Work

	Reactor A	Reactor B
d, mm	1	2
D, mm	4.8	9.6
H, mm	3.8	7.6
Z, mm	5.8	11.6
K, mm	20	40
δ, mm	2	4

Table 2. Initial Concentration of Reagents and Their Ratio

Case #	c_A, mol/m^3	c_B, mol/m^3
1	100	100
2	500	500
3	100	500
4	200	100
5	500	100
6	800	100

The flow rates of the feed streams were varied between 3 and 120 ml/min. The flow field in CIJRs is often characterized by the jet Reynolds number:

$$\mathrm{Re} = \frac{u_1 d}{\nu} \tag{1}$$

where u_1 is the jet velocity, d is the jet diameter, and ν is the kinematic viscosity of water (that is, 1.0×10^{-6} m^2/s). The range of flow rates reported above results in a range of jet Reynolds number of about 50 to 3000 for the two reactors. It should be highlighted here that in all the experiments the flow rates of the two feed streams were kept equal to each other.

Different series of experiments have been carried out by varying the initial concentrations of barium chloride (c_A) and sodium sulfate (c_B) in the feed streams, and a summary is reported in Table 2. First, initial concentrations were kept equal to each other ($c_A = c_B = 100$ mol/m^3, run #1 and $c_A = c_B = 500$ mol/m^3, run #2); then the effect of sulfate ion excess ($c_A = 100$ mol/m^3, $c_B = 500$ mol/m^3, run #3) and the effect of barium ion excess ($c_B = 100$ mol/m^3 and $c_A = 200$ mol/m^3 run #4, $c_A = 500$ mol/m^3 run #5, $c_A = 800$ mol/m^3 run #6) were investigated.

Samples at the outlet of the reactor were taken and diluted with bi-distilled water in order to freeze the reaction. The PSD was measured by laser light scattering (Coulter LS 230) either immediately or after half an hour to verify the solution stability. Samples were filtered with cellulose nitrate membrane filters (MicroFiltrationSystems, pore size 100 nm), dried at 120°C, and prepared for Scanning Electron Microcopy (SEM) and X-ray diffraction in order to investigate particle morphology and crystallinity. The average crystallite size was measured by X-ray diffraction (Philips PW3830) and calculated using the Scherrer equation[20,21]:

$$d_S = \frac{0.9\lambda}{B \cos\vartheta_B} \tag{2}$$

where d_s is the average crystallite size, 0.9 is a shape factor, λ is the wavelength of the X-ray radiation (0.15406 nm), and B (radiands) is the broadening of the peak at the diffraction angle θ_B and can be calculated from:

$$B = (W_{1/2}^2 - W_{1/2,0}^2)^{1/2} \tag{3}$$

where $W_{1/2}^2$ is the experimentally observed breadth and $W_{1/2,0}^2$ is the instrumental breadth of a peak that exhibits no broadening beyond the inherent instrumental peak width.

Calculation of the Characteristic Mixing and Reaction Time Scales

The final goal of our work is the development of a fully predictive CFD-based precipitation model that could be profitably used to design and scale-up precipitation reactors. Such a model must describe accurately the flow and turbulence fields, and the interaction between chemical reaction and turbulence, and must use accurate kinetic expressions for nucleation, growth, and aggregation. Barium sulfate precipitation has been studied for many years now, and nucleation and growth kinetics are better known, although some fundamental aspects still have to be completely understood, especially concerning nucleation. Moreover, for the aggregation kernel, and especially for the aggregation efficiency, no reliable kinetic expressions exist. Therefore, further investigations are needed in order to derive a fully predictive model without fitting parameters. In this work we are interested in a preliminary validation of our work that includes the calculation of mixing and reaction time scales, in order to treat and interpret experimental data. It is interesting to highlight here that since the main uncertainties lie in the aggregation step, the calculation of the characteristic reaction time is still feasible and reliable; in fact, as already reported, the characteristic reaction time does not depend on aggregation but on nucleation and growth only. In what follows, the techniques used to calculate characteristic mixing and reaction time scales are presented.

Characteristic mixing time

In order to estimate mixing efficiencies and characteristic mixing time scales, the CIJR was simulated using CFD. The flow field and the turbulence field were described using the standard Reynolds-Averaged Navier-Stokes approach. Moreover, transport equations for the mean mixture fraction, $\langle\xi\rangle$, and the mixture fraction variance, $\langle\xi'^2\rangle$, were also solved. The mixture fraction is a non reacting scalar that ranges from zero to one and contains information concerning the amount of reactants coming from one inlet with respect to the other.[22] The mean mixture fraction transport equation is (where repeated indices imply summation):

$$\frac{\partial\langle\xi\rangle}{\partial t} + \langle u_i\rangle \frac{\partial\langle\xi\rangle}{\partial x_i} = \frac{\partial}{\partial x_i}\left((\Gamma + \Gamma_t)\frac{\partial\langle\xi\rangle}{\partial x_i}\right), \tag{4}$$

where $\langle u_i\rangle$ is the Reynolds-averaged velocity in the i^{th} direction, x_i is the spatial coordinate in the i^{th} direction, Γ is the molecular diffusivity, and Γ_t is the turbulent diffusivity, which can be calculated by using the definition of turbulent Schmidt number and the Boussinesq hypothesis, resulting in the following expression:

$$\Gamma_t = \frac{C_\mu}{Sc^t}\frac{k^2}{\varepsilon}, \tag{5}$$

where C_μ is a constant equal to 0.09, Sc^t is the turbulent Schmidt number usually fixed equal to 0.7, k is the turbulent kinetic energy, and ε is the turbulent energy dissipation rate.

However, the mean mixture fraction calculated with Eq. 4 does not contain information about turbulent scalar fluctuations at a scale smaller than the grid scale. This information can be obtained by deriving the transport equation for the mixture fraction variance $\langle \xi'^2 \rangle$ as explained by Fox[22]:

$$\frac{\partial \langle \xi'^2 \rangle}{\partial t} + \langle u_i \rangle \frac{\partial \langle \xi'^2 \rangle}{\partial x_i} = \frac{\partial}{\partial x_i}\left((\Gamma + \Gamma_t) \frac{\partial \langle \xi'^2 \rangle}{\partial x_i} \right) + 2\Gamma_t \frac{\partial \langle \xi \rangle}{\partial x_i}\frac{\partial \langle \xi \rangle}{\partial x_i} - 2\Gamma \left\langle \frac{\partial \xi'}{\partial x_i}\frac{\partial \xi'}{\partial x_i} \right\rangle, \quad (6)$$

where ξ' is the fluctuating value of the mixture fraction. As can be seen, the variance is produced by large scale gradients (that is, second term on the righthand side of Eq. 6) and dissipated by small scale gradients (that is, third term on the righthand side of Eq. 6). In order to solve the equation, a closure for the dissipation term is needed. As explained by Fox,[22] this can be done by extracting this quantity from the scalar energy spectrum, resulting in:

$$\langle \varepsilon_\xi \rangle = 2\Gamma \left\langle \frac{\partial \xi'}{\partial x_i}\frac{\partial \xi'}{\partial x_i} \right\rangle = 2\,\frac{C_\phi}{2}\,\frac{\varepsilon}{k}\,\langle \xi'^2 \rangle = 2\gamma \langle \xi'^2 \rangle \quad (7)$$

where γ is usually referred to as the micro-mixing rate; and C_ϕ is a constant that for fully turbulent flows is equal to two, but in general, for a fluid with Schmidt number greater than 1000, can be calculated as a function of the local Reynolds number[23] (Re_1):

$$C_\phi = \sum_{n=0}^{6} a_n (\log_{10} \mathrm{Re}_1)^n \quad (8)$$

valid for $Re_1 > 0.2$, where $a_0 = 0.4093$, $a_1 = 6015$, $a_2 = 0.5851$, $a_3 = 0.09472$, $a_4 = -0.3903$, $a_5 = 0.1461$, and $a_6 = -0.01604$, and where:

$$\mathrm{Re}_1 = \frac{k}{(\varepsilon \nu)^{1/2}}. \quad (9)$$

From Eq. 7 it is possible to derive a characteristic time t_s for the mixture fraction variance decay:

$$t_\phi = \frac{1}{2\gamma} = \frac{1}{C_\phi}\frac{k}{\varepsilon}. \quad (10)$$

This characteristic time can be interpreted as the micro-mixing time, namely, the time required for a blob of fluid to achieve complete mixing at the molecular level, or, in other words, to destroy micro-scale gradients present at the sub-grid scale level of the CFD simulation.

This characteristic time does not account for the time required to destroy macro-scale gradients. Macro-scale segregation can be quantified by defining a macro-scale variance:

$$\langle \xi'^2 \rangle_L = (\langle \xi \rangle - \bar{\xi})^2 \quad (11)$$

where $\bar{\xi}$ is the mixture fraction value when complete mixing has occurred and, for example, for equal flow rates is equal to 0.5. The relative transport equation is[23]:

$$\frac{\partial \langle \xi'^2 \rangle_L}{\partial t} + \langle u_i \rangle \frac{\partial \langle \xi'^2 \rangle_L}{\partial x_i} = \frac{\partial}{\partial x_i}\left((\Gamma + \Gamma_t) \frac{\partial \langle \xi'^2 \rangle_L}{\partial x_i} \right) - 2\Gamma_t \frac{\partial \langle \xi \rangle}{\partial x_i}\frac{\partial \langle \xi \rangle}{\partial x_i}. \quad (12)$$

As can be seen, the macro-scale variance does not have a production term and reaches its maximum value in the inlet streams and decays to zero with a characteristic time that can be calculated as follows:

$$t_L = \frac{\langle \xi'^2 \rangle_L}{2\Gamma_t \dfrac{\partial \langle \xi \rangle}{\partial x_i}\dfrac{\partial \langle \xi \rangle}{\partial x_i}}. \quad (13)$$

This characteristic time is the time required to destroy large-scale gradients and corresponds to the action of mean velocities and turbulent dispersion and in the classical notation of chemical reaction engineering the process is usually referred to as macro- and meso-mixing. The total mixing time t_m can be evaluated as the summation of the micro-mixing time t_ϕ (see Eq. 10) and the macro- and meso-mixing time t_L (see Eq. 13) and according to the operating conditions one of them can be the controlling one.[23] For example, it has been shown in our previous work[24] that in a semi-batch reactor for very fast injections, macro-mixing is the controlling resistance ($t_L \gg t_\phi$), whereas for very slow injections micro-mixing is the limiting phenomenon ($t_\phi \gg t_L$).

Precipitation time scales

In order to evaluate the characteristic time scale of the precipitation process, the kinetics of the relevant phenomena involved must be quantified. Several kinetic expressions have been reported over the past decades.[10,25,26] However, as already explained, only nucleation and growth determine the characteristic reaction time. It is important to remember that the precipitation model is used here only to calculate the characteristic reaction time, and although different kinetic expressions result in very different PSDs, they result in similar reaction times. The homogeneous nucleation rate is usually expressed as the number of nuclei produced per unit volume and unit time (#/m^{3}s) and can be estimated using the classical nucleation theory.[11-13,27] The super-saturation has to be calculated taking into account the fact that the ionic solution does not behave as an ideal thermodynamic system due to the high ionic strength under which precipitation usually occurs. This can be done through the activity coefficient for the barium-sulfate ion pair, which can be calculated following the approach by Bromley[28] and successive corrections by Monnin.[29]

For particle growth, several mechanisms and kinetics expressions have been proposed[30,31]; however, at high super-saturation it can be considered diffusion controlled and, moreover, for very small particles (sub-micron) the theoretical limit value of Sherwood number equal to two is reached and the expression proposed by Schwarzer and Peukert[12] can be used.

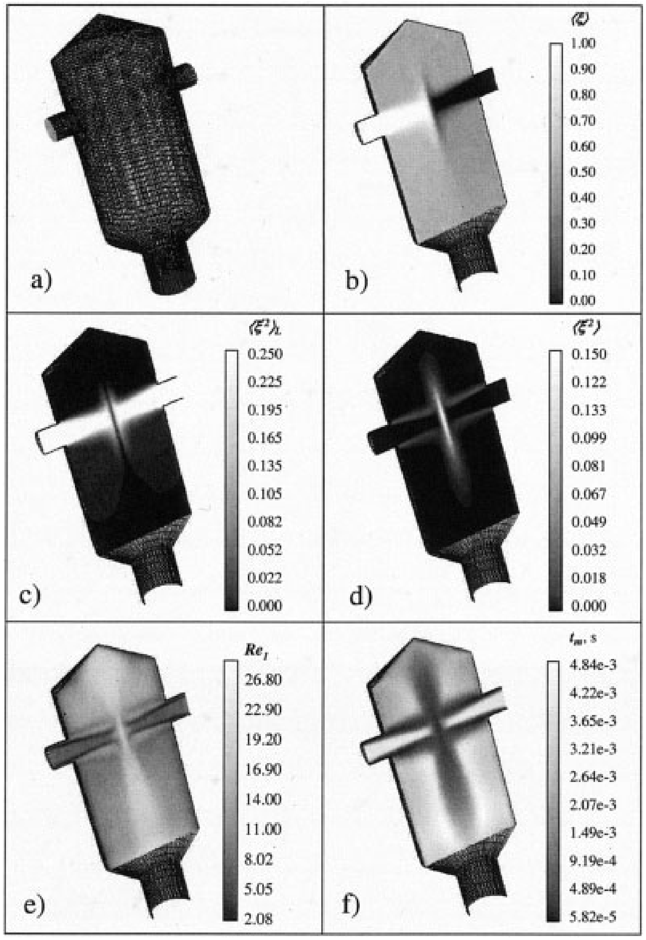

Figure 2. Results for the small reactor (d = 1 mm) for Re = 1500.

(a) Three dimensional grid used in the simulations, (b) mixture fraction contour plot, (c) large-scale mixture fraction variance, (d) micro-scale mixture fraction variance, (e) local Reynolds number, (f) local mixing time.

As already reported, in this simple calculation we are just interested in quantifying the characteristic time scale of precipitation and comparing this quantity with the mixing time scale. The reaction time scale is calculated assuming perfect macro- and micro-mixing; the population balance equation is solved resorting to the quadrature method of moments,[32] coupled with the material balance equations for barium and sulfate ions assuming spherical and compact crystals. Readers interested in the details of the precipitation model and the kinetics expressions can refer to the work of Schwarzer and Peukert.[12]

Numerical Details

As already reported, the CIJR was modeled with the CFD code Fluent using the Reynolds-Averaged Navier-Stokes (RANS) approach. Both geometries (that is, $d = 1$ mm and $d = 2$ mm) were considered, and the three dimensional unstructured grid with 81,104 cells used in the simulations is reported in Figure 2a. It is worth noting that the final grid was obtained after considering different grid densities and different meshing strategies and the solution obtained was grid independent for both reactor geometries. Different turbulence models and different near-wall treatments were considered. The lack of experimental data concerning the flow and turbulent fields makes it very difficult to discern between different modeling choices. However, preliminary results from another work, concerning modeling of fast parallel competitive reactions in confined impinging jet reactors, and comparison with Large Eddy Simulation results, seem to suggest that the Reynolds Stress Model (RSM) with enhanced wall treatment gives the best predictions. This hypothesis seems reasonable; in fact, the RSM is very suitable for modeling complex flow with strong anisotropy. Moreover, the small reactor volume and the fact that the jets are confined within walls at a short distance probably require an accurate treatment of the near wall regions, instead of the usual wall function approach. Nevertheless, only quantitative and extensive comparison with experimental data concerning the flow and turbulence fields can give a definitive answer in discerning among possible modeling choices. The range of jet Reynolds numbers investigated is the same as in the experiments, although very low Reynolds numbers have not been simulated since the flow was laminar or in the laminar to turbulent transition where the turbulence models are very well known to fail.

The solution of transport equations for the mean mixture fraction and mixture fraction variance, as well as the calculation of mixing times, was carried out with user-defined subroutines. Simulations were considered converged when the normalized residuals were smaller than 10^{-6}. These convergence criteria were used for flow, turbulence, mean mixture fraction, and mixture fraction variance fields.

Results and Discussion

Precipitation experiments at different jet Reynolds numbers and reactant concentrations required being frozen in order to carry out PSD measurements and filtrations for SEM observation and X-ray diffraction. The precipitation reaction at the reactor outlet was frozen with a simple dilution with bi-distilled water. Different dilution ratios were tested, namely, 10 ml of solution from the reactor outlet in 100 ml of bi-distilled water, 10 ml in 500 ml, and 5 ml in 750 ml. After dilution samples were gently stirred and one PSD measurement was immediately carried out, then successive measurements were carried out every 5-10 minutes and compared. Dilution was shown to be effective; in fact, after dilution the suspension was found to be stable up to 10 minutes. Results also show that, in general, the higher the dilution ratio, the more stable is the suspension, leading to the conclusion that the best choice would be to work with very diluted suspensions; however, this can be a source of errors in the light scattering measurement, where a minimum amount of solid particles is needed to have "enough statistics" to reconstruct the PSD from light scattering data. A reasonable trade-off was the dilution of 10 ml in 100 ml of bi-distilled water, and all the results presented hereinafter were obtained operating with this ratio.

Effect of jet Reynolds number and reactant concentration

Let us analyze the dependence of the precipitate characteristics on mixing conditions for the small reactor (d = 1 mm). First, the cases with equal reactant concentrations (case #1: $c_A = c_B = 100$ mol/m^3 and case #2: $c_A = c_B = 500$ mol/m^3) and

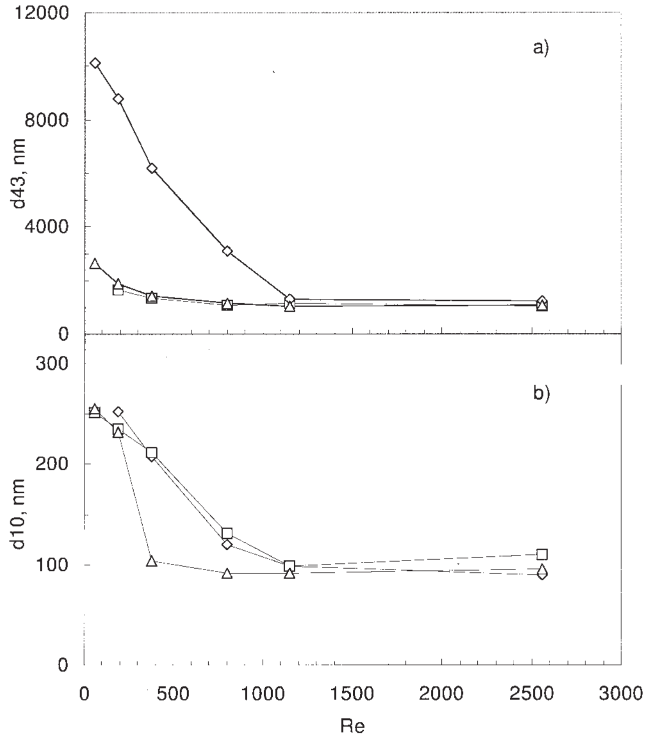

Figure 3. Effect of the jet Reynolds number *Re* on: (a) the volume-averaged particle size d_{43}, and (b) the number-averaged particle size d_{10}.

Squares: c_B = 100 mol/m^3 and c_A = 100 mol/m^3 (see case #1 Table 2); diamonds: c_B = 500 mol/m^3 and c_A = 500 mol/m^3 (see case #2 Table 2); triangles: c_A = 100 mol/m^3 and c_B = 500 mol/m^3 (see case #3 Table 2) for the small reactor (d = 1 mm).

with sulfate ion excess (case #3: c_A = 100 mol/m^3 and c_B = 500 mol/m^3) will be considered. Results for these cases are reported in Figure 3, in terms of the volume-averaged particle size (Figure 3a) and in terms of the number-averaged particle size (Figure 3b), whereas results for the other cases and for the bigger reactor (d = 2 mm) will be discussed later. As a general comment, it is possible to state that at low jet Reynolds numbers, mixing is poor and the overall super-saturation is low, resulting in low nucleation rates and in bigger particles. Increasing *Re* mixing becomes more efficient; super-saturation is built up faster, resulting in higher nucleation rates and smaller particles. However, when the characteristic mixing time scale has reached the reaction time scale, further improvement in mixing efficiency does not affect the PSD. It is interesting to highlight that for low initial reactant concentrations $c_A = c_B$ = 100 mol/m^3 (case #1) this occurs when *Re* reaches 800; whereas if both barium and sulfate ion initial concentrations are increased up to $c_A = c_B$ = 500 mol/m^3 (case #2), this occurs at higher jet Reynolds numbers, proving that at higher concentrations the chemical reaction is faster and, therefore, the mixing time scale equals the precipitation time scale at higher jet Reynolds numbers. Very similar results were obtained with an excess of sulfate with respect to barium initial concentration, as can be clearly seen in Figure 3a (c_A = 100 mol/m^3 and c_B = 500 mol/m^3 case #3 of Table 2).

In Figure 4a the PSDs for three jet Reynolds numbers are reported and it can be seen that they are all bimodal, evidencing that aggregation has taken place. From SEM observations (see, for example, Figures 5a and 5b) it seems that aggregation occurs from the early stages of nucleation and growth until the very last instants before exiting the reactor outlet, resulting in two different types of aggregates. The first ones are very compact and present significant re-crystallization on the bridges between primary particles, whereas the second ones are bigger, with more open structures, and seem to be constituted by aggregation of several of the smaller compact aggregates. This could probably be explained by the fact that in the very beginning super-saturation is very high and produces a huge number of nuclei that quickly aggregate and grow, forming compact and small aggregates. When the super-saturation reaches lower values, the nucleation rate is negligible, and the already formed compact aggregates can further grow and some of them can stick together, forming a second, less numerous population of bigger aggregates. The two different phenomena can still be traced by the bimodal PSDs, where the first peak seems to be representative of the first population of smaller aggregates made of primary particles, whereas the second peak is probably representative of the second population of bigger aggregates.

The characteristic size of the first population of small and compact aggregates can be quantified by d_{10}, namely, the ratio of the 1st and 0th moments of the PSD, or, in other words, the

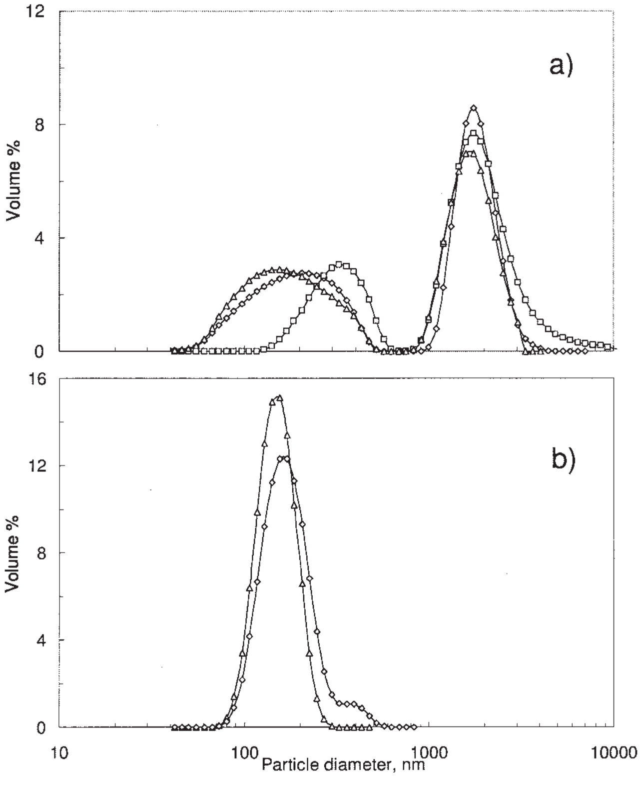

Figure 4. PSDs at the reactor outlet for different jet Reynolds numbers: *Re* = 188 (open squares), *Re* = 1180 (open diamonds), and *Re* = 2296 (open triangles) for the small reactor.

(a) Case #1: $c_A = c_B$ = 100 mol/m^3; (b) case #6: c_A = 800 mol/m^3 and c_B = 100 mol/m^3.

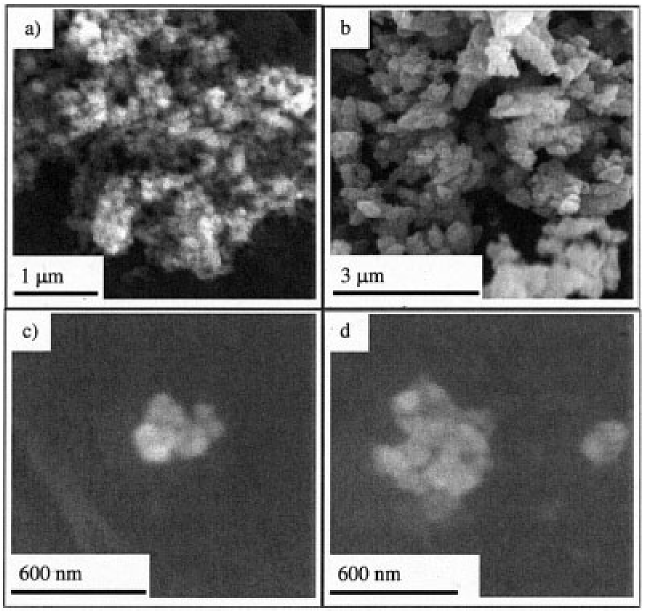

Figure 5. Particle morphology obtained in the small reactor d = 1 mm at different operating conditions.

(a) $Re = 1180$; $c_A = c_B = 100$ mol/m^3; (b) $Re = 188$; $c_A = c_B = 500$ mol/m^3; (c) $Re = 188$; $c_A = 800$ mol/m^3 $c_B = 100$ mol/m^3; (d) $Re = 1180$; $c_A = 800$ mol/m^3 $c_B = 100$ mol/m^3.

mean particle size with respect to the number distribution function. In fact, in the calculation of d_{10}, small particles "count" more because they outnumber the big ones. The mean particle size based on the volume distribution (that is, d_{43}) is instead more influenced by the presence of the second population of bigger aggregates; in fact, in the volume distribution, bigger particles count more because of their bigger size and volume.

The effect of the jet Reynolds number for cases #1, #2, and #3 on d_{10} is reported in Figure 3b, where it is possible to see that an increase in Re causes a reduction of the number-averaged particle size from 300 nm down to 100 nm. Comparison of Figures 3a and 3b shows a consistent behavior; nevertheless, for cases #1 and #3, where the limiting reactant concentration is the same, an increase in Re seems to have a bigger effect on the position of the first peak (reproduced by d_{10}) than on the second peak, which seems to be centered around 2-4 μm notwithstanding the value of Re. This is confirmed by Figure 4a, where the PSDs at different Re are reported for case #1 only. The fact that Re and, therefore, mixing intensity does not seem to affect the position of the second peak (see cases #1 and #3), except where the initial concentration for both reactants is higher (case #2), probably implies that in this latter condition the final size of the bigger particles is dictated by aggregation driven by Brownian motions insensitive to turbulence intensity.

Let us now discuss the three series of experiments conducted with an excess of barium with respect to sulfate initial concentrations (that is, $c_B = 100$ mol/m^3 and $c_A = 200$, 500, and 800 mol/m^3, see cases #4, #5, and #6 of Table 2). Results are summarized in Figure 6, and it is possible to see that at low jet Reynolds numbers because of poor mixing, the mean particle size is about 2-3 μm, but increasing the jet Reynolds number up to 2000, the particle size is reduced down to about 80-100 nm. In fact, as shown in our previous work,[12] barium excess reduces aggregation, shielding particles with electrostatic repulsion; for these three cases also, SEM observations confirmed the smaller particle size and the weaker effect of particle aggregation (see Figures 5c and 5d). SEM observations seem to show that only the first type of small and compact aggregates are formed at high Reynolds numbers. In fact, particles are constituted by primary particles of about 20-40 nm that aggregate to form very small aggregates of about 80-100 nm of size. The compactness of the aggregates proves that they are formed by the first type of aggregation and, moreover, in the analyzed samples there was no trace of the big and sparse aggregates. This is also confirmed by the PSDs reported in Figure 4b that are monomodal and by the fact that for these distributions d_{43} was very similar to d_{10}.

As already explained, the average size of primary particles can be retrieved from X-ray diffraction patterns. Using the Scherrer equation (see Eq. 2), it was possible to derive the mean crystallite size and its dependence against the jet Reynolds number for the small reactor (d = 1 mm) and for $c_A = 800$ mol/m^3 and $c_B = 100$ mol/m^3, as reported in Figure 7. It is important to remember that this measurement is affected by many experimental errors and although the correction for the instrumental broadening was accounted for, the value of the mean crystallite size should be regarded as an indication of its order of magnitude. However, the trend indicated by the experimental data is very clear and shows that by increasing the jet Reynolds number, mixing is improved and smaller primary particles (see Figure 7) and smaller aggregates (see Figure 6) are produced.

The precipitation experiments for the six investigated cases were repeated, in a similar range of jet Reynolds number, for the big reactor (d = 2 mm). Particle characterization showed very similar results. The effect of the jet Reynolds number is always to reduce the particle size until a constant value is reached. For the first cases, #1, #2, and #3, particle aggregation was very strong, resulting in big particles, whereas working

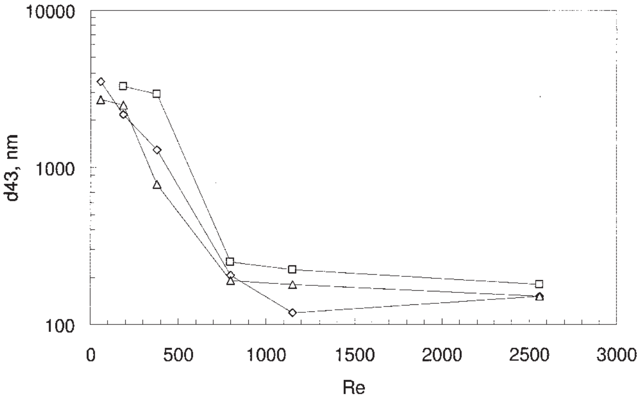

Figure 6. Effect of the jet Reynolds number *Re* on the mean particle size d_{43}.

Squares: $c_B = 100$ mol/m^3 and $c_A = 200$ mol/m^3 (see case #4 Table 2); diamonds: $c_B = 100$ mol/m^3 and $c_A = 500$ mol/m^3 (see case #5 Table 2); triangles: $c_B = 100$ mol/m^3 and $c_A = 800$ mol/m^3 (see case #6 Table 2) for the small reactor (d = 1 mm).

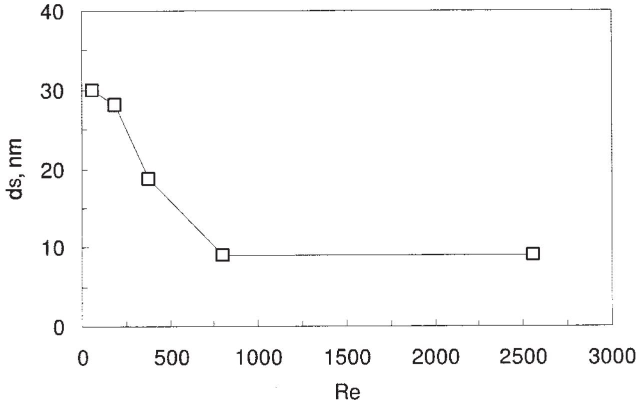

Figure 7. Mean crystallite size versus the jet Reynolds number calculated with the Schrerrer equation from X-ray measurements for the small reactor ($d = 1$ mm) and for $c_A = 800$ mol/m^3 and $c_B = 100$ mol/m^3.

with barium excess (that is, cases #4, #5, and # 6), particle aggregation was attenuated and smaller sub-micron particles were produced. For brevity, the results will not be presented here but in the following sections, when the scale-up criteria will be explained and discussed.

Characteristic mixing and precipitation time scales

Mixing time scales in the confined impinging jet reactor have been quantified by investigating turbulent transport of the mixture fraction, as already explained. In Figure 2b the contour plot of the mixture fraction is reported for the small reactor ($d = 1$ mm) and for $Re = 1500$. The mixture fraction is assumed to be equal to one in the barium feed stream and zero in the sulfate one. As can be seen, at $Re = 1500$, mixing is quite effective. In fact, in most of the reactor, the mixture fraction is equal to 0.5, which corresponds to the condition of perfect mixing with equal flow rates. This can be clearly seen also in Figure 2c, where the large-scale variance is reported. This quantity reaches its maximum value in the inlets (that is, 0.25), and it is then destroyed by convection and turbulent dispersion, resulting in values very close to zero at the outlet. Very similar results were obtained at the other Reynolds numbers investigated, and a quantitative comparison will be discussed later in terms of characteristic mixing time scales.

Also, the transport equation for the mixture fraction variance was solved. It is useful to remember here that the mixture fraction variance represents fluctuations around the mean value due to turbulent mixing on time and length scales smaller than the grid size. The contour plot of the mixture fraction variance is reported in Figure 2d. As can be seen, the variance is zero in the inlet streams and, since it is produced by mean mixture fraction gradients, it reaches its maximum in the impinging plane.

The local Reynolds number Re_l is reported in Figure 2e always for the small reactor ($d = 1$ mm) and for jet Reynolds number equal to 1500. The local Reynolds number is an indicator of the turbulence level; in fact, for $Re_l > 100$ the flow is assumed to be fully turbulent, and for $Re_1 < 10$ the flow is in the laminar to turbulent transition. As can be seen, Re_1 is relatively high in the area around the impinging plane but it is smaller than 10 in the regions near the walls. The situation is very similar for the other jet Reynolds numbers and for the big reactor, and the results seem to confirm that the flow is fully turbulent only for very high jet Reynolds number (that is, $Re > 3000$).

The local value of the total mixing time t_m is reported in Figure 2f and, averaging over the reactor volume, a mean representative value can be found. The dependence of the volume-averaged mixing time versus the jet Reynolds number is reported for the two investigated geometries in Figure 8. As can be seen, increasing the jet Reynolds number one order of magnitude (that is, from 200 to 2000), the mixing time decreases and for the small reactor ($d = 1$ mm) varies from 50 ms to 2 ms, whereas for the big reactor ($d = 2$ mm) it varies from 100 ms to 5 ms. It should be highlighted here that the mean residence time varies between 40 ms and 1 ms for the small reactor, and varies between 3 s and 200 ms for the big reactor. The mean residence time scales with Re^{-1} and their dependency with respect to the jet Reynolds number are also reported in Figure 8, along with the dependency of the mixing time calculated with a correlation found in literature[17] that scales with $Re^{-3/2}$. It is useful to recall that at low jet Reynolds numbers ($Re < 1500$), the flow is very far from being fully turbulent and, therefore, CFD results should be treated with caution.

For a similar geometry, but a smaller reactor, the mixing time was calculated, obtaining similar results.[23] In general, it is very difficult to individuate a simple correlation for the mixing time since it contains contributions from macro- and micro-scale phenomena. For example, from Figure 8 it is possible to observe a dependence very close to $Re^{-3/2}$ for low jet Reynolds numbers and close to Re^{-1} at higher jet Reynolds numbers. Moreover, if the mixing time scales of the big reactor ($d = 2$ mm) and of the small one ($d = 1$ mm) are compared, a factor equal to two is found, in contrast with the correlation from literature,[17] which predicts that the mixing time scale of reac-

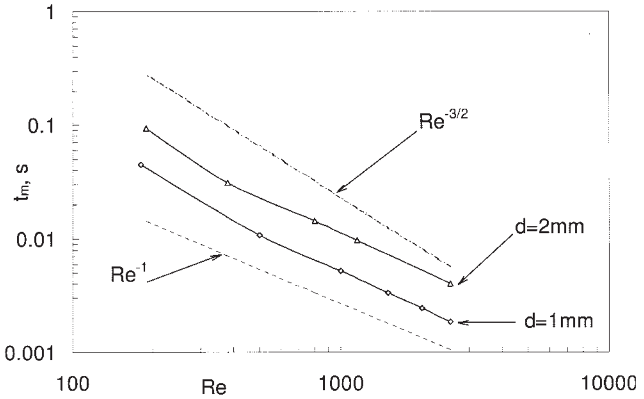

Figure 8. Dependence of volume-averaged mixing time in the CIJR over the jet Reynolds number for the small ($d = 1$ mm) and the big reactor ($d = 2$ mm).

The line corresponding to the dependence of the mean residence time $\propto Re^{-1}$ and the mixing time calculated by Johnson and Prud'homme (2003[2]) $\propto Re^{-3/2}$ are reported for comparison.

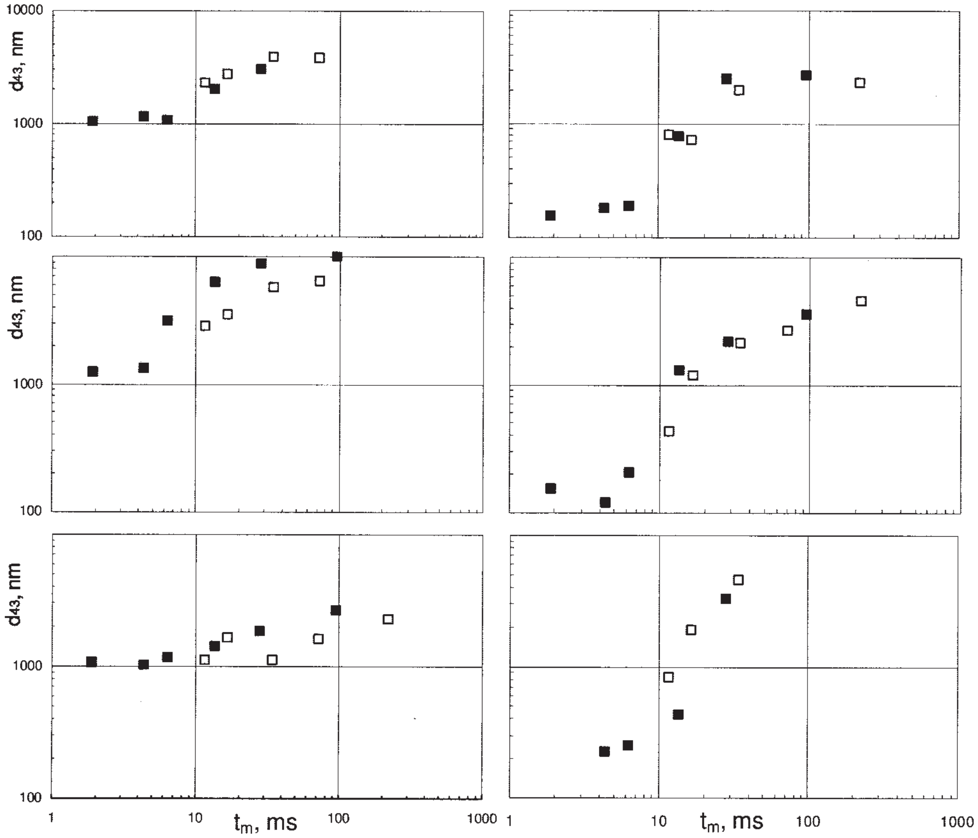

Figure 9. Mean particle size vs. mixing time for the small reactor (filled symbols) and the big reactor (open squares) and for the six cases investigated.

(a) Case #1: $c_A = c_B = 100$ mol/m^3; (b) case #2: $c_A = c_B = 500$ mol/m^3; (c) case #3: $c_A = 100$ mol/m^3 and $c_B = 500$ mol/m^3; (d) case #4: $c_B = 100$ mol/m^3 and $c_A = 200$ mol/m^3; (e) case #5: $c_B = 100$ mol/m^3 and $c_A = 500$ mol/m^3; (f) case #6: $c_B = 100$ mol/m^3 and c_A 800 mol/m^3.

tors with similar geometries but different jet diameters scales with $d^{1/2}$.

If the mixing times reported in Figure 8 are used to represent the data for the small and big reactors for the six cases, the results reported in Figure 9 are obtained. As can be seen, the mean particle size is well correlated by the mixing time and, in fact, the data referring to the small and big reactors collapse in one single curve, showing that the calculated mixing time is representative of the real mixing dynamics. Of course, the data reported in different plots refer to different chemical reaction rates and, therefore, the characteristic precipitation time scale must be included in order to obtain a single master curve. It must also be taken into account that aggregation occurs in addition to the competition between nucleation and molecular growth, smoothing down the particle size dependency over mixing conditions for sub-micron particles. Therefore, only comparisons between experimental data where the aggregation rate is comparable are significant.

Using the simple precipitation model previously described, it is possible to determine the characteristic time scale for precipitation: for case #1 ($c_A = c_B = 100$ mol/m^3) a characteristic reaction time of about 7.7 ms was calculated; for case #2 ($c_A = c_B = 500$ mol/m^3) about 1.7 ms; and for case #3 ($c_A = 100$ mol/m^3 and $c_B = 500$ mol/m^3) about 3.2 ms. As expected, by increasing the initial reactant concentration, the reaction time decreases from 7.7 ms down to 3.2 and 1.7 ms. The three cases with barium excess $c_B = 100$ mol/m^3 and $c_A = 200$, 500, and 800 mol/m^3 (see case #4, case #5, and case #6 of Table 2) resulted in similar reaction times of about 3 ms, 2.6 ms, and 2.4 ms, respectively. As already reported, the use of different kinetic expressions or different correlations for the activity coefficients may result in slightly different time scales, but the order to magnitude and the trends are similar.

Of course, the implementation of the precipitation model in the CFD code would result in a fully predictive tool; however, especially for precipitation kinetics, an extensive comparison and validation is required. This is beyond the scope of this work as it is currently under investigation and will be reported elsewhere.

The mean particle size at the reactor outlet for the small and big reactors can be correlated by using the Damköhler number, namely, the ratio between the mixing and the precipitation time calculated with the CFD and with the precipitation model. Results are reported in Figures 10a and 10b, for high aggregation rates (cases #1, #2, and #3) and low aggregation rates (cases #4, #5, and #6) and, as can be seen, experiments referring to different operating conditions lay on the same curve.

When working with high aggregation rates (see Figure 10a) and when mixing is much slower than the chemical reaction ($Da \gg 1$), particles are big (8-10 μm); whereas only when mixing is faster than the chemical reaction ($Da < 1$) are particles small ($\approx$1 μm). Also, for small values of Da, a

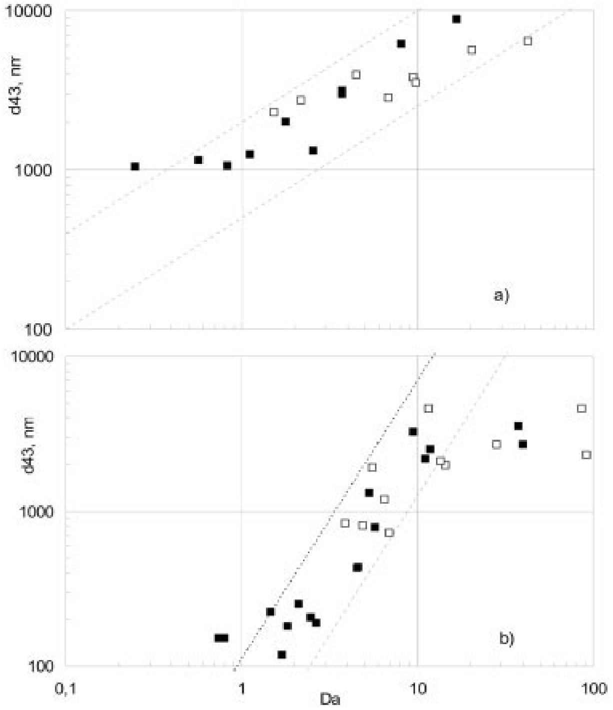

Figure 10. Mean particle size vs. the Damköhler number for the small and big reactors.

(a) High aggregation efficiency (cases #1, #2, and #3); (b) reduced aggregation efficiency (cases #4, #5, and #6).

minimum value is reached and further improvement in mixing does not affect the final particle size. As already said, in these cases particle size cannot go below 1 μm because of extensive aggregation.

When working with barium ion excess (cases #4, #5, and #6), the aggregation efficiency is strongly reduced and, therefore, particles have a lower tendency to aggregate. Results are reported in Figure 10b and, as can be seen, also in this case experiments referring to different operating conditions collapse into one single curve. It is interesting to note that the slope of the mean particle size vs. Da is higher in this case (that is, 1.8) than in the previous one (that is, 0.7) due to the absence of aggregation. Also in this case, when mixing is much slower than the chemical reaction ($Da \gg 1$), particles are quite big (4-5 μm); whereas only when mixing is faster than the chemical reaction ($Da < 1$) do particles reach sub-micron sizes ($\approx$100 nm), confirming what was anticipated in the Introduction concerning the important role of mixing in producing sub-micron particles.

Conclusions and Next Steps

In this work we have investigated turbulent precipitation in CIJRs for the production of nanoparticles and, in particular, we highlighted the role that turbulent mixing plays in reactor scale up. Results show that attention should always be devoted to the chemical "recipe" suitable for obtaining a specific product, for example, in this case, operating with only the excess of one reactant, sub-micron particles were produced. Nevertheless, the interplay between mixing and precipitation is crucial; in fact, our results show that with the same chemical "recipe" and only changing mixing conditions, the mean particle size was reduced from a few microns down to 80 nanometers.

This interplay becomes extremely important during scale-up of these reactors. Scale-up can be carried out by extracting characteristic time scales for mixing and reaction from CFD simulations and from a simple precipitation model. Experimental data seem to correlate well when these time scales are used. The calculation of the time scales with the CFD and precipitation models is, of course, more complex and time consuming than standard calculations based on simple algebraic correlations[17]; however, this approach has been shown to be more reliable and accurate.

The ultimate goal of our work is the implementation of the precipitation model in the CFD code and its validation against experimental data, resulting in a fully predictive model, completely free from fitting and tuning parameters.

Acknowledgments

The authors would like to thank Prof. Rodney Fox for useful discussions and for sharing the preprints of his article on this subject. The financial support of the Ministry of Education, University and Research for the fellowship of one of the authors (LR) is gratefully acknowledged.

Literature Cited

1. Johnson BK, Prud'homme RK. Flash nanoprecipitation of organic actives and block copolymers using a confined impinging jets mixer. *Australian J Chem.* 2003;56:1021-1024.
2. Johnson BK, Prud'homme RK. Mechanism for rapid self-assembly of block copolymer nanoparticles. *Phys Rev Letters.* 2003;91:1183021-1183024.
3. Horn D, Rieger J. Organic nanoparticles in the aqueous phase—theory, experiment, and use. *Angewandte Chemie - International Ed.* 2001; 40:4330-4361.
4. Brinker CJ, Scherer GW. Sol-Gel Science—The Physics and Chemistry of Sol-Gel Processing. San Diego: Academic Press; 1990.
5. Rivallin M, Benmami M, Kanaev A, Gaunand A. Sol-gel reactor with rapid micromixing modelling and measurements of titanium oxide nano-particle growth. *Chem Eng Research Design.* 2005;83–1A:67-74.
6. Dirksen JA, Ring TA. Fundamentals of crystallization: kinetics effect of particle size distribution and morphology. *Chem Eng Sci.* 1991;46: 2389-2427.
7. Marchisio DL, Soos M, Sefcik J, Morbidelli M. Role of turbulent shear rate distribution in aggregation and breakage processes. *AIChE J.* 2006;52:158-173.
8. Mersmann A. Crystallization and precipitation. *Chem Eng Proc.* 1999; 38:345-353.
9. Elimelech M, Jia X, Gregory J, Williams RA. *Particle Deposition and Aggregation: Measurement, Modelling and Simulation*. Woburn MA: Butterworth-Heinemann; 1998.
10. Zukoski CF, Rosenbaum DF, Zamora PC. Aggregation in precipitation reactions: stability of primary particles. *Chem Eng Research Design.* 1996;74:723-731.
11. Schwarzer H-C, Peukert W. Experimental investigation into the influence of mixing on nanoparticle precipitation. *Chem Eng Tech.* 2002; 25:657-661.
12. Schwarzer H-C, Peukert W. Combined experimental/numerical study on the precipitation of nanoparticles. *AIChE J.* 2004;50:3234-3247.
13. Schwarzer H-C, Peukert W. Prediction of aggregation kinetics based on surface properties of nanoparticles. *Chem Eng Sci.* 2005;60:11-25.
14. Marchisio DL, Barresi AA, Garbero M. Nucleation, growth, and agglomeration in barium sulfate turbulent precipitation. *AIChE J.* 2002;48:2039-2050.
15. Judat B, Kind M. Morphology and internal structure of barium—derivation of a new growth mechanism. *J Colloid Interface Sci.* 2004; 269:341-353.
16. Mahajan AJ, Kirwan DJ. Micromixing effects in a two-impinging-jets precipitator. *AIChE J.* 1996;42:1801-1814.

17. Johnson BK, Prud'homme RK. Chemical processing and micromixing in confined impinging jets. *AIChE J.* 2003;49:2264-2282.
18. Schaer E, Guichardon P, Falk L, Plasari E. Determination of local energy dissipation rates in impinging jets by a chemical reaction method. *Chem Eng J.* 1999;72:125-138.
19. Bénet N, Muhr H, Plasari E, Rousseaux JM. New technologies for the precipitation of solid particles with controlled properties. *Powder Tech.* 2002;128:93-98.
20. Eckert Jr JO, Hung-Houston CC, Gersten BL, Lencka MM, Riman RE. Kinetics and mechanisms of hydrothermal synthesis of barium titanate. *J Am Ceramic Soc.* 1996;79:2929-2939.
21. Scherrer P. *Nachrichten von der Gesellschaft der Wissenschaften zu Göttingen.* 1918;2:98-100.
22. Fox RO. *Computational Models for Turbulent Reacting Flows*. Cambridge: Cambridge University Press; 2003.
23. Ying L, Fox RO. CFD predictions for chemical processing in a confined impinging-jets reactor. *AIChE J.* 2006;52:731-744.
24. Marchisio DL, Barresi AA. CFD simulation of mixing and reaction: the relevance of the micromixing model. *Chem Eng Sci.* 2003;58: 3579-3587.
25. Aoun M, Plasari E, David R, Villermaux J. Are barium sulfate kinetics sufficiently known for testing precipitation reaction models? *Chem Eng Sci.* 1996;51:2449-2458.
26. Baldyga J, Podgorska W, Pohorecki R. Mixing-precipitation model with application to double feed semi-batch precipitation. *Chem Eng Sci.* 1995;50:1281-1300.
27. Mersmann A. *Crystallization Technology Handbook 2nd ed*. New York: Marcel Dekker; 2000.
28. Bromley LA. Thermodynamic properties of strong electrolytes in aqueous solutions. *AIChE J.* 1973;19:313-320.
29. Monnin C. A thermodynamic model for solubility of barite and celestite in electrolyte solutions and seawater to 200°C and 1 kbar. *Chem Geology.* 1999;153:187-197.
30. Nielsen AE. Electrolyte crystal growth mechanism. *J Crystal Growth.* 1984;67:289-310.
31. Nielsen AE, Toft JM. Electrolyte crystal growth kinetics. *J Crystal Growth.* 1984;67:278-288.
32. McGraw R. Description of aerosol dynamics by the quadrature method of moments. *Aerosol Sc Tech.* 1997;27:255-265.

Manuscript received Aug. 2, 2005, and revision received Dec. 12, 2005.